JOURNAL OF GEOPHYSICAL RESEARCH, VOL. 106, NO. E12, PAGES 32,863–32,877, DECEMBER 25, 2001

Assimilation of Mars Global Surveyor atmospheric temperature data into a general circulation model

Kate Q. Zhang, Andrew P. Ingersoll,[1] and David M. Kass
Jet Propulsion Laboratory, California Institute of Technology, Pasadena, California, USA

John C. Pearl, Michael D. Smith, and Barney J. Conrath
Goddard Space Flight Center, Greenbelt, Maryland, USA

Robert M. Haberle
Ames Research Center, Moffett Field, California, USA

Abstract. We examined the observed temperature data from Thermal Emission Spectrometer (TES) between heliocentric longitude $L_s = 141°$ and 146° (~10 Martian days in northern summer) during the mapping phase, then compared them with the simulated results using the NASA/Ames Mars general circulation model. Both show a strong polar vortex at the winter pole, higher equatorial temperatures near the ground and larger tropospheric lapse rates during daytime than at night. However, the simulation is colder than the observation at the bottom and top of the atmosphere and warmer in the middle. The highest wave activities are found in the polar front in both the simulations and the observations, but it is at a much higher altitude in the former. Experiments show that larger dust opacity improves the temperature field in the lower atmospheric levels. Using a steady state Kalman filter, we attempted to obtain a model state that is consistent with the observations. The assimilation did achieve better agreement with the observations overall, especially over the north pole. However, it is hard to make any further improvement. Dust opacity is the key factor in determining the temperature field; correcting temperature alone improves the spatial and temporal variations, it degrades the mean state in the south pole. Assimilation cannot improve the simulation further, unless more realistic dust opacity and its vertical profile are considered.

1. Introduction

One important aspect of Mars exploration involves understanding the weather and climate of the planet, a goal that is significant on its own and that helps in planning successful future missions. The Mars Global Surveyor (MGS) enabled us to take a close look at the Martian surface and atmosphere. TES is one of the instruments on board. It looks into the atmosphere and sends back 10 radiance measurements of bands in the infrared, from which 20 variables, including atmospheric temperatures at 16 levels, surface temperature, optical depth, etc., are derived. Pressure at ground level is taken from an off-line calculation using a Mars general circulation model (MGCM) (a detailed description of the retrieval procedure is given by *Conrath et al.*, [2000]). The temperature measurements used here are limited to nadir views of the instrument, which orbits the planet ~12 times per Martian day (hereafter sol) at ~30° intervals of longitude.

General circulation models produce 4-dimensional solutions given the initial state, topography, forcing, and model parameters. One such model is the NASA/Ames MGCM, described by *Pollack et al.* [1990] and *Haberle et al.* [1993]. The idea here is to assimilate the observed temperature profiles into the MGCM and bring the model solution closer to the observations. We thus obtain a continuous and more realistic description of temperature and winds for the global Martian atmosphere, even though only temperature has been observed over a restricted region of space and time [*Conrath et al.*, 2000]. We can then examine the solution against the observational data to find out how to improve the model, as well as the retrieval procedure. Finally, it becomes possible to answer questions such as what the prominent variability on Mars is.

[1]Division of Geology and Planetary Sciences, California Institute of Technology, Pasadena, California, USA

Paper number 2000JE001330.
0148-0227/01/2000JE001330$09.00

2. Observations

The spacecraft entered its mapping phase in late northern summer and has been continuously surveying the surface and atmosphere of Mars. Readers are referred to *Christensen et al.* [1992, 1998] for more thorough descriptions of TES.

2.1. TES data

The raw data are the radiance of the surface and atmosphere system at different wavelengths (6-50 μm). They are then inverted to temperature profiles [*Conrath et al.*, 2000]. Although TES can make both nadir and limb observations, only data from the nadir views were processed and used for our analysis here. Readers are referred to *Conrath et al.* [2000] and *Smith et al.*[2000*a*, *b*] for more detailed descriptions of how the inversion was done. The processed TES data are put into 10-sol-long files, which contain information on time, location in longitude and latitude, dust opacity to visible light, quality flag, and temperature values and its corresponding pressure levels above the surface. The first 10-sol spans from heliocentric longitude L_s=141.0 to 146.0 and is northern summer. As an example, the footprint tracks for ascending (i.e., dayside) and descending (i.e., nightside) orbits during the first 10-sol period were plotted in Figure 1 for the 2.9-mbar pressure level. There are some gaps near Olympus Mons, which is due to its topography. There are other gaps, most often at high latitudes, where the instrument was dedicated to limb sounding rather than nadir sounding. The MGS ascending node is at 1400 local time (LT), and its descending node is at 0200 LT. The resulting footprint tracks slant from southeast to northwest on the dayside and from northeast to southwest on the nightside. Each orbit crosses the equator (7/87)x360°

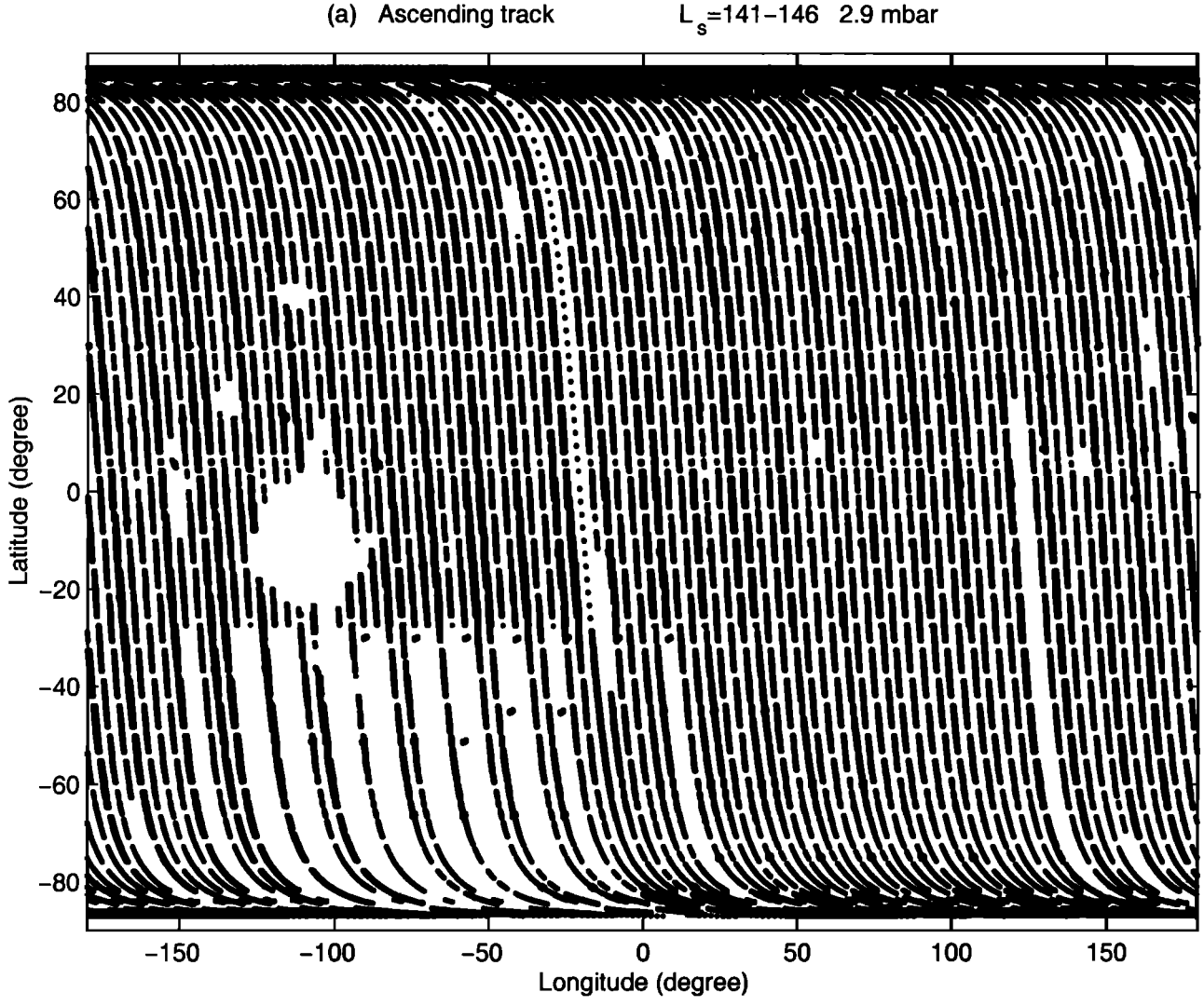

Figure 1. The footprint tracks of the 10-sol observations ($L_s = 141° - 146°$) at 2.9 mbar pressure level for (a) ascending orbits (1400 LT) and (b) descending orbits (0200 LT). Each dot represents one observational point. The discontinuities indicate missing observations because the instrument was turned off, the topography was sufficiently high that TES results were considered unreliable, or because limb observations were being made.

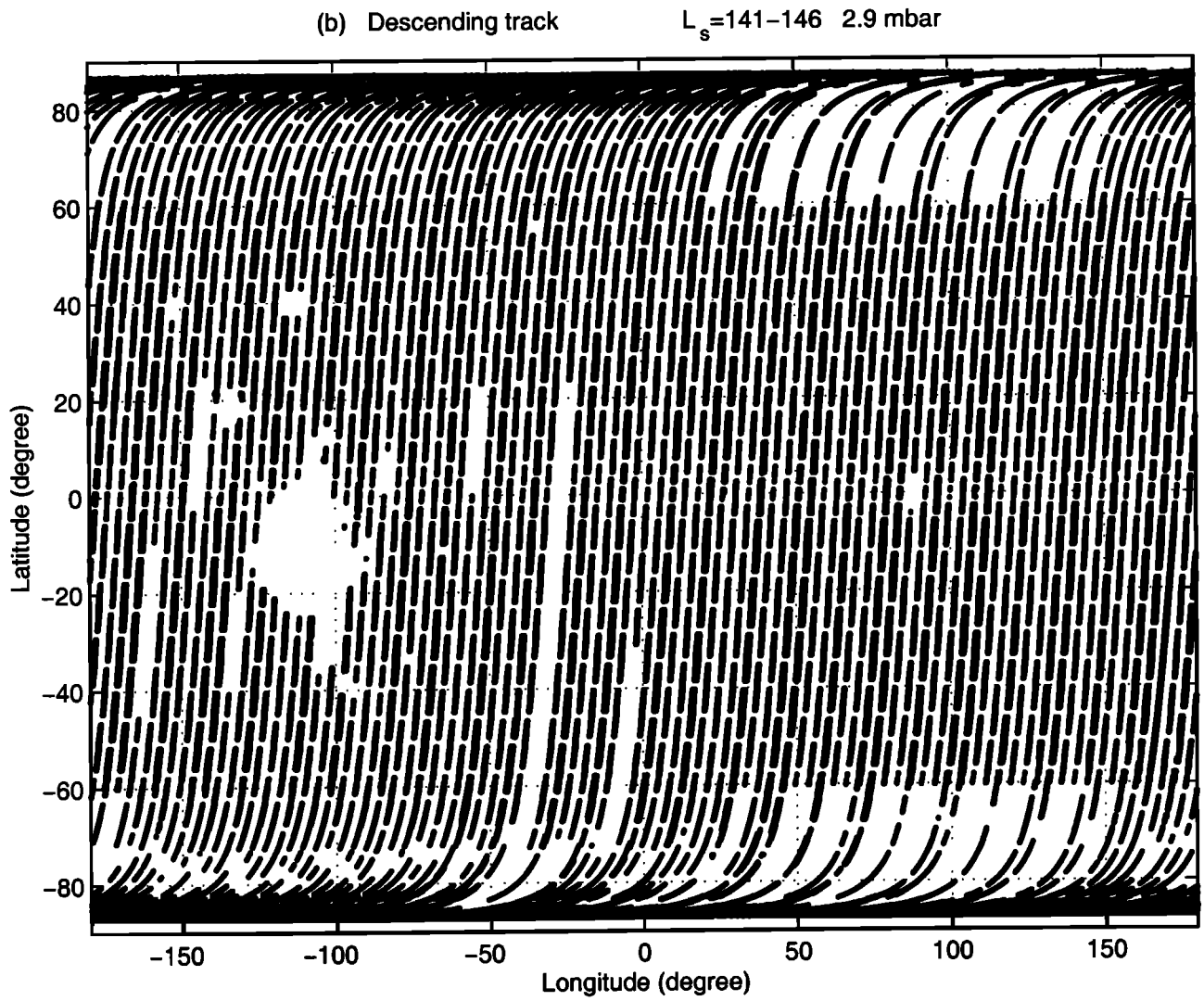

Figure 1. (continued)

to the west of the previous orbit (~29° to the west), which means that the orbits repeat (namely, cross the same longitudes) after 7 sols (i.e., 87 orbits).

Information about dust opacity to visible light is extracted from the data and averaged along latitudes and longitudes, respectively (Figure 2). The meridional mean varies little with longitudes, while the longitudinal mean is the largest at high latitudes and is minimum at low latitudes. The global mean of dust opacity to visible light is 0.17, making the total dust opacity twice as large, 0.34.

2.2. Results

As a first step, the whole globe was divided into 5° by 5° bins and all the data that fell into each bin were collected, note that these data were not taken simultaneously, but at two local times, 1400 or 0200. Then, data in the bins at the same latitude and at the same pressure level were averaged and treated as zonal means, and standard deviations associated with the zonal means were taken for either ascending or descending tracks,

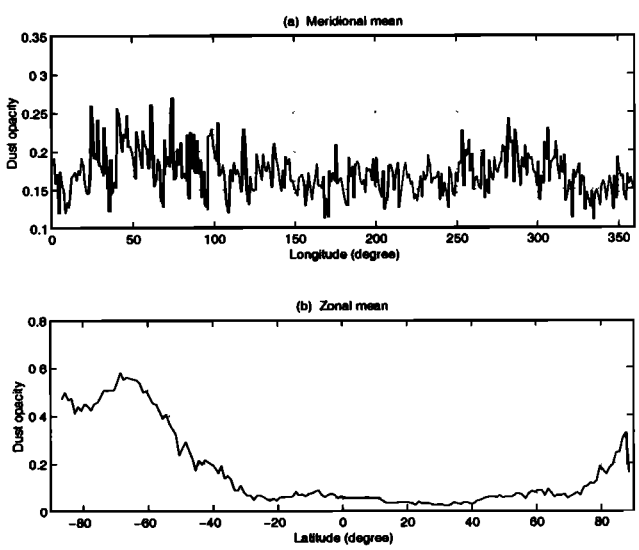

Figure 2. Observed dust opacity along the footprint tracks of MGS during the 10-sol period: (a) meridional mean and (b) latitudinal mean. Note largest dust opacity is found at high latitudes in the south.

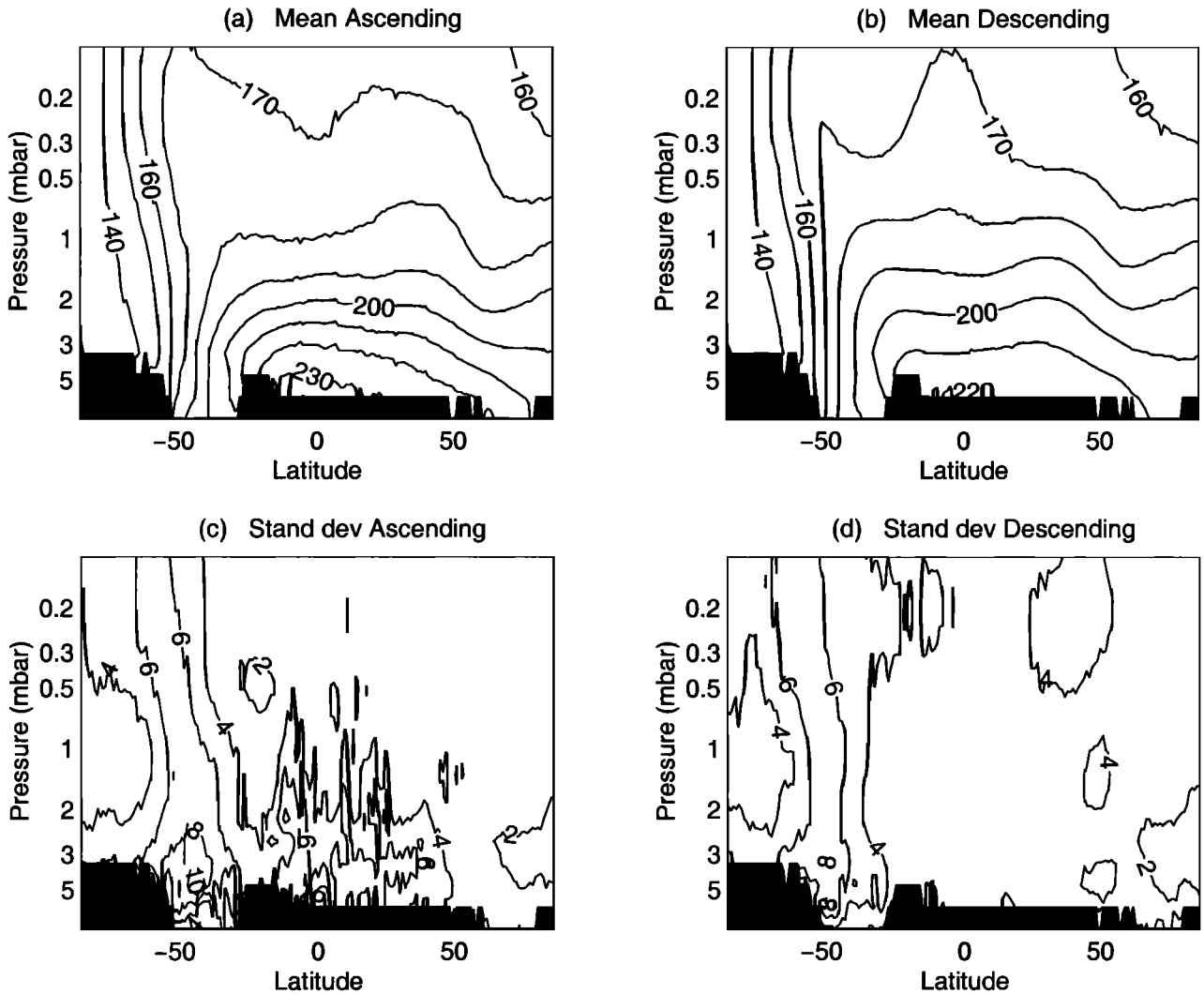

Figure 3. Zonal means and standard deviations of observed temperature for every vertical level and 5° resolution in latitude for $L_s = 141° - 146°$ of mapping phase (orbit 02555-02674) along (a and c) ascending tracks and (b and d) descending tracks. Units are °K. Black areas mark regions of no data.

respectively. The primary contributors to the standard deviations [*Conrath et al.*, 2000] are wave activities, seasonal evolution of the temperature field during the period of the averaging, and retrieval errors. The total random errors in individual retrievals is of the order of 2°K, and standard deviations larger than 4-5°K are considered significant wave activities. Considering 10 day-span data as instantaneous may introduce artifacts which can be examined with the model results if this is the case (see section below).

The zonal mean temperatures and the standard deviations associated with the zonal means along ascending and descending tracks were plotted in Figure 3. In the winter hemisphere, a strong polar front was observed at high southern latitudes, associated with the polar vortex. The wall of this vortex can be seen from the almost vertically standing isotherms near the south pole during the day as well as the night. At low latitudes the tropospheric lapse rate is stronger at daytime, and zonal mean temperature maximum is ~10° higher at daytime than at night. This is because the Martian atmosphere has very low thermal inertia and can be heated up easily. On the equator the 170° isotherm shows opposite phase during the day and at night, a feature related to thermal tides.

The wave activity as a function of latitude is dramatically different during the day from that at night. Figures 3c and d show zonally averaged standard deviations of the 10-sol temperature for ascending and descending tracks, respectively. During the day the wave activities are generally high near the ground at low and middle latitudes. It is worth noting that part of such high activities might be unrealistic, since it is difficult to retrieve low-level temperature over cold ground. The daytime activity is high throughout the troposphere and in the polar front, with a maximum of 10° at 5 mbar pressure level. The fact that the lower atmosphere is highly active at 1400 LT is consistent with its high temperature but may be compounded by low level retrieval problems as well as spatial and temporal variations. At night the

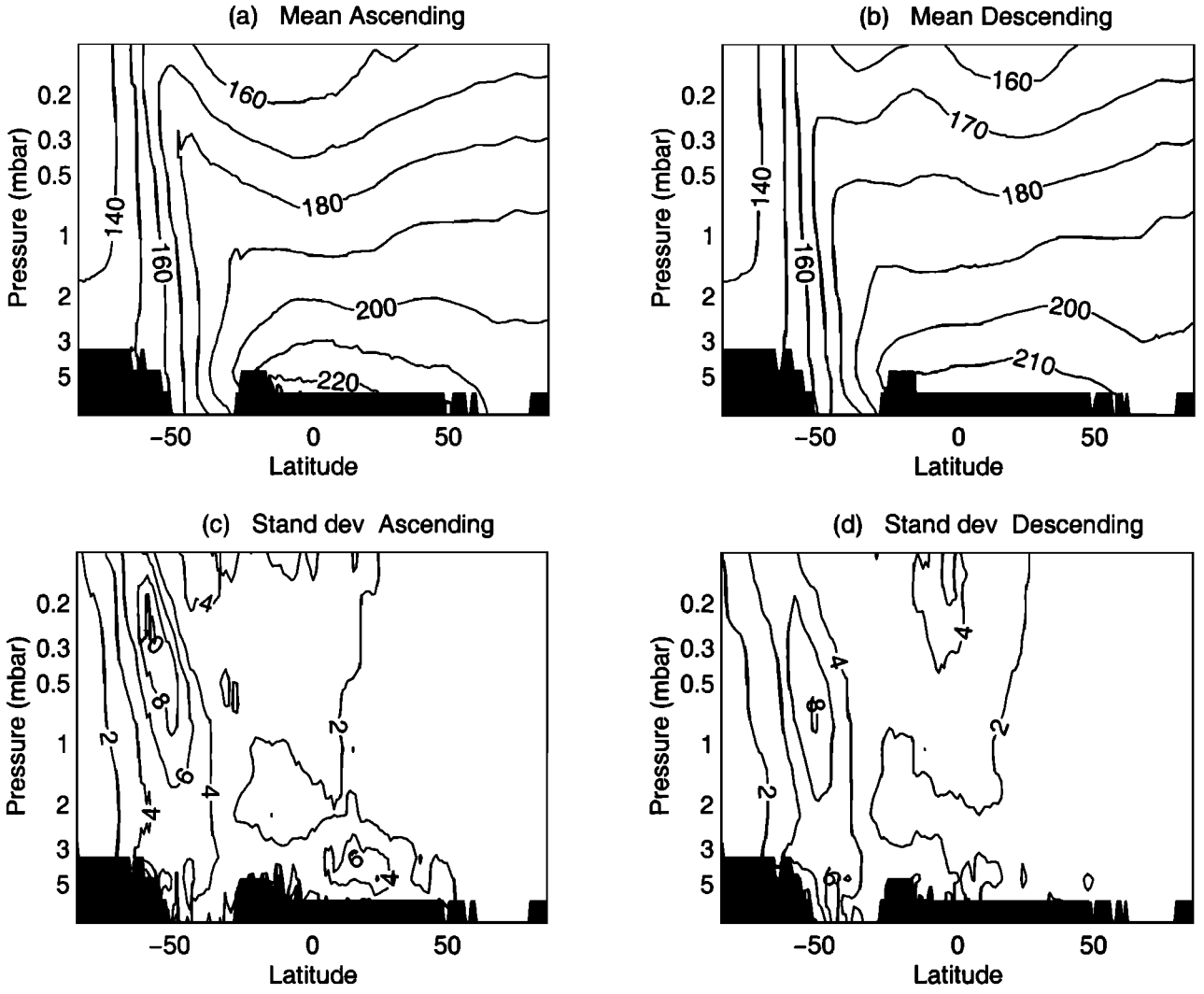

Figure 4. Zonal means and standard deviations of temperature from baseline simulation T34F0 sampled on data along (a and c) ascending tracks and (b and d) descending tracks. Units are °K. Black areas mark regions of no data.

atmosphere is less active overall, wave activities in the polar front remains most active, although the amplitude has weakened compared to that at daytime. The north pole remains quiet, while activity at the equator has become uniform over height in the absence of sunlight.

3. Simulation

Misfits between the observation and simulation exist, since models are not perfect and observational errors cannot be avoided. Here we compare the temperature values produced in a MGCM with those retrieved from TES data. In the next section we assimilate the retrieved temperature values into the MGCM to find out to what degree the model solution can be improved.

3.1. Description of the Model

We use the Mars general circulation model developed and maintained at Ames Research Center. The resolution is 9° in longitude and 7.5° in latitude. There are 13 levels in the vertical. A sigma coordinate system is used to better resolve the topography. The model assumes that the dust is uniformly distributed with respect to the gas, so the optical depth is proportional to surface pressure. The global average of observed dust amount for the 10-sol period determines the optical depth in the model. We spun up the model from a motionless state for 90 sols, after which the atmosphere has reached a quasi-equilibrium. The final state on sol 90 was used as the initial condition for our simulation and assimilation experiments which both last 10 sols as data. We designed the experiment so that the heliocentric longitude L_s at sol 90 is the same as the beginning of sol 1 in the observations. Then we sampled the simulated Martian atmosphere along the same tracks as the MGS and treated the model-produced data exactly the same way as the observational data. Recent topography from Mars Orbiter Laser Altimeter (MOLA) is interpolated onto our model grid points and used in the experiments [*Smith et al.*, 1999].

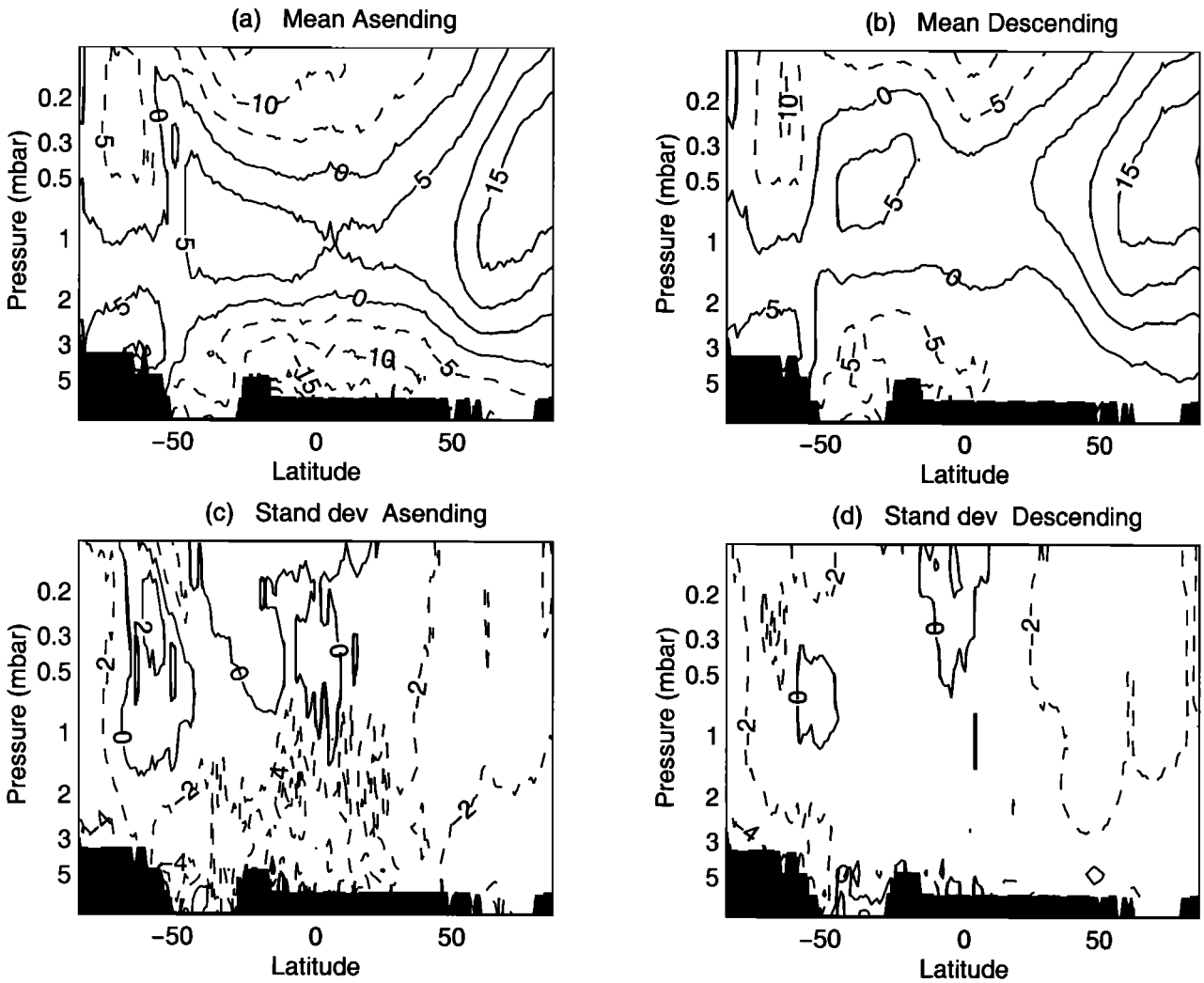

Figure 5. Difference between direct simulation T34F0 and observations in zonal means and standard deviations of temperature, sampled along (a and c) ascending tracks and (b and d) descending tracks. Units are °K. Black areas mark regions of no data.

3.2. Model Results

The temperature field of the baseline simulation with $\tau = 0.34$ (hereinafter referred to as simulation T34F0) is sampled along the trajectories of MGS for 10 sols, and then the zonal means in latitude and standard deviations in both longitude and latitude for the model results sampled on data were calculated (Figure 4). Features similar to those of the observations can be found: the polar front is observed at similar latitudes near the south pole, the tropospheric lapse rate at 1400 LT is stronger than that at 0200 LT, and the maximum temperature at 1400 LT is ~10° higher than that at 0200 LT. A note-worthy difference is the direction of the isotherms above the summer polar region: they are upward toward the north pole in the simulation but downward in the observations.

At 1400 LT (ascending) the waves in the simulated atmosphere are most active in the polar front as well as near the ground at low latitudes. At 0200 LT (descending), the waves remain active only in the polar front and has become quiet in the lower atmosphere. Like

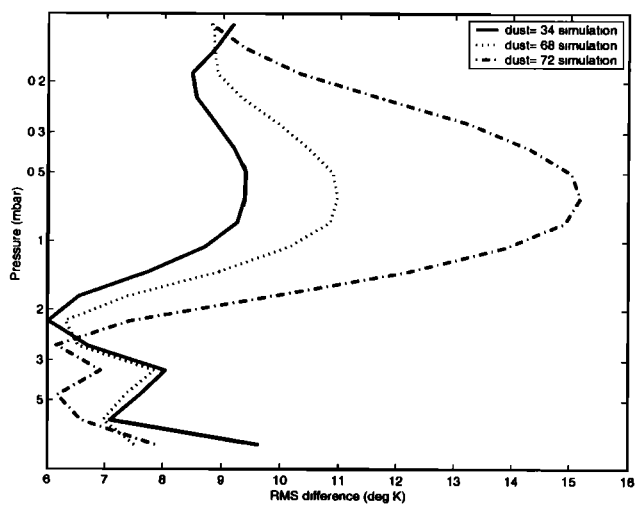

Figure 6. Temperature RMS difference between baseline simulations and observations as a function of pressure. The RMS is computed over longitude and latitude. The solid line is for simulation T34F0, the dotted line for simulation T68F0, and the dash-dotted line is for simulation T72F0.

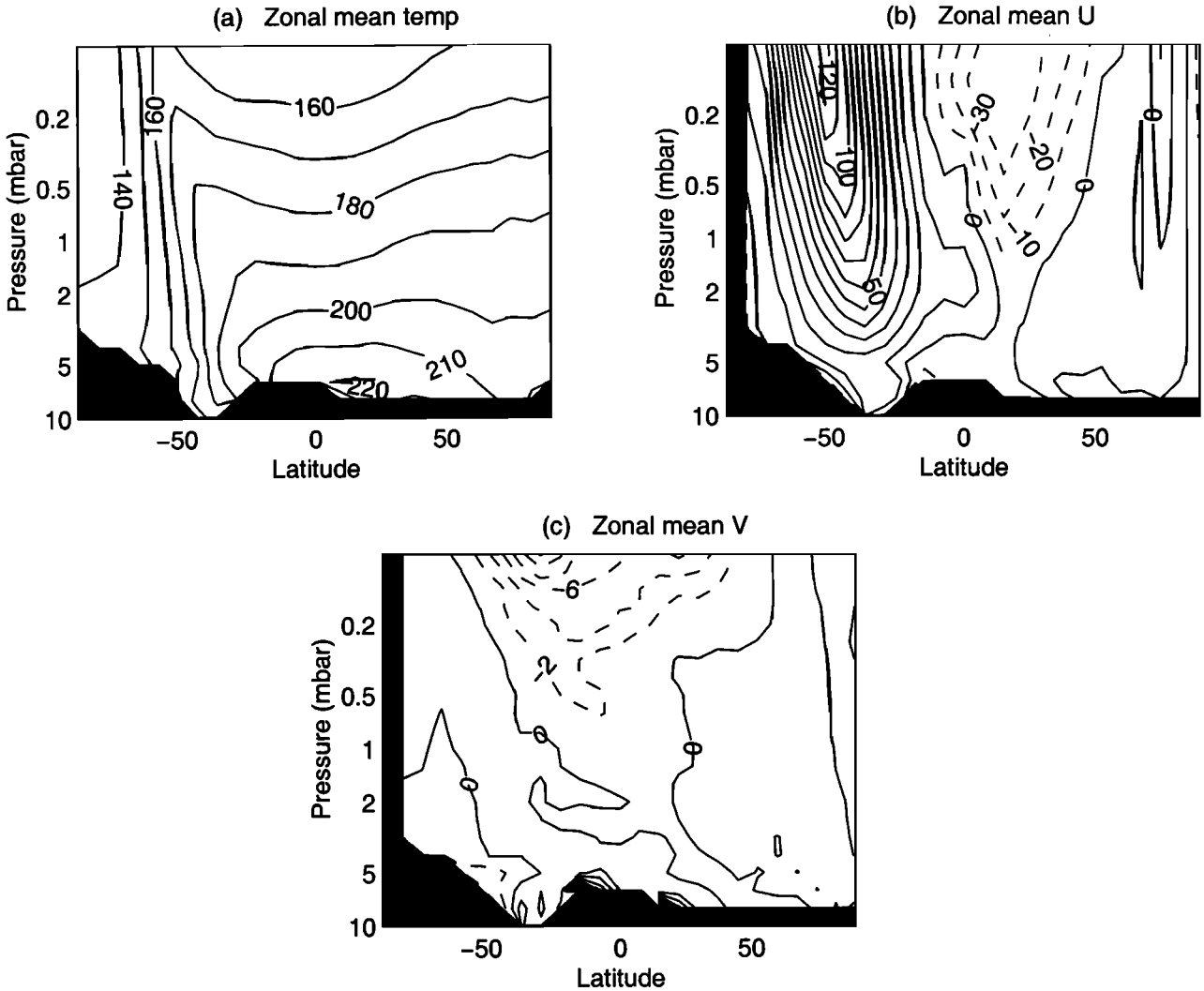

Figure 7. Zonally averaged (a) temperature, (b) zonal velocity, and (c) meridional velocity for the entire 10-sol mean atmosphere in baseline simulation T34F0. Black areas mark regions of no data.

in observations, the wave activities in the polar vortex are higher during the day than at night. The wave activities exist at latitudes similar to those of the observations and with a magnitude similar to those of the observations, but the peak is at much higher altitudes.

The difference in zonal means and standard deviations between simulation T34F0 and the observations are shown in Figure 5. The simulated temperature right above the ground is colder than the observations for both day and night, by 15° at 1400 LT and 10° at 0200 LT. The simulated temperature is colder at the top, but warmer in the middle of the atmosphere at low and middle latitudes. Inside the polar vortex the simulated temperature is 5° colder above 1 mbar level and 10° warmer below. In the northern polar region the simulation gives a higher temperature above the ground with a maximum of 15°. The simulated activity is generally weaker in the northern hemisphere and inside the polar vortex for both day and night. Inside the polar front wave activity is higher above 2 mbar level in the simulated atmosphere than observations, especially along the ascending tracks.

To understand the impact of dust on model solution, two additional baseline simulations were done with τ=0.68 and 0.72. The RMS difference in latitude and longitude between the baseline simulations and the observations was plotted in Figure 6 as a function of pressure. Simulated results using the dust opacity deduced from observations are by far the closest to the observed temperatures above 2.5 mbar level, but give the worst fit below. It is plausible that the vertical profile of the dust is unrealistic, larger dust opacity is required in lower atmosphere to produce the observed temperatures. This figure suggests that the temperature field in the model is sensitive to the dust opacity as well as the vertical profile. For these additional simulations, the horizontal structure remains similar to the one in Figure 5, but the amplitude of the difference has increased over the whole atmosphere.

Figure 7 shows the zonally averaged temperature,

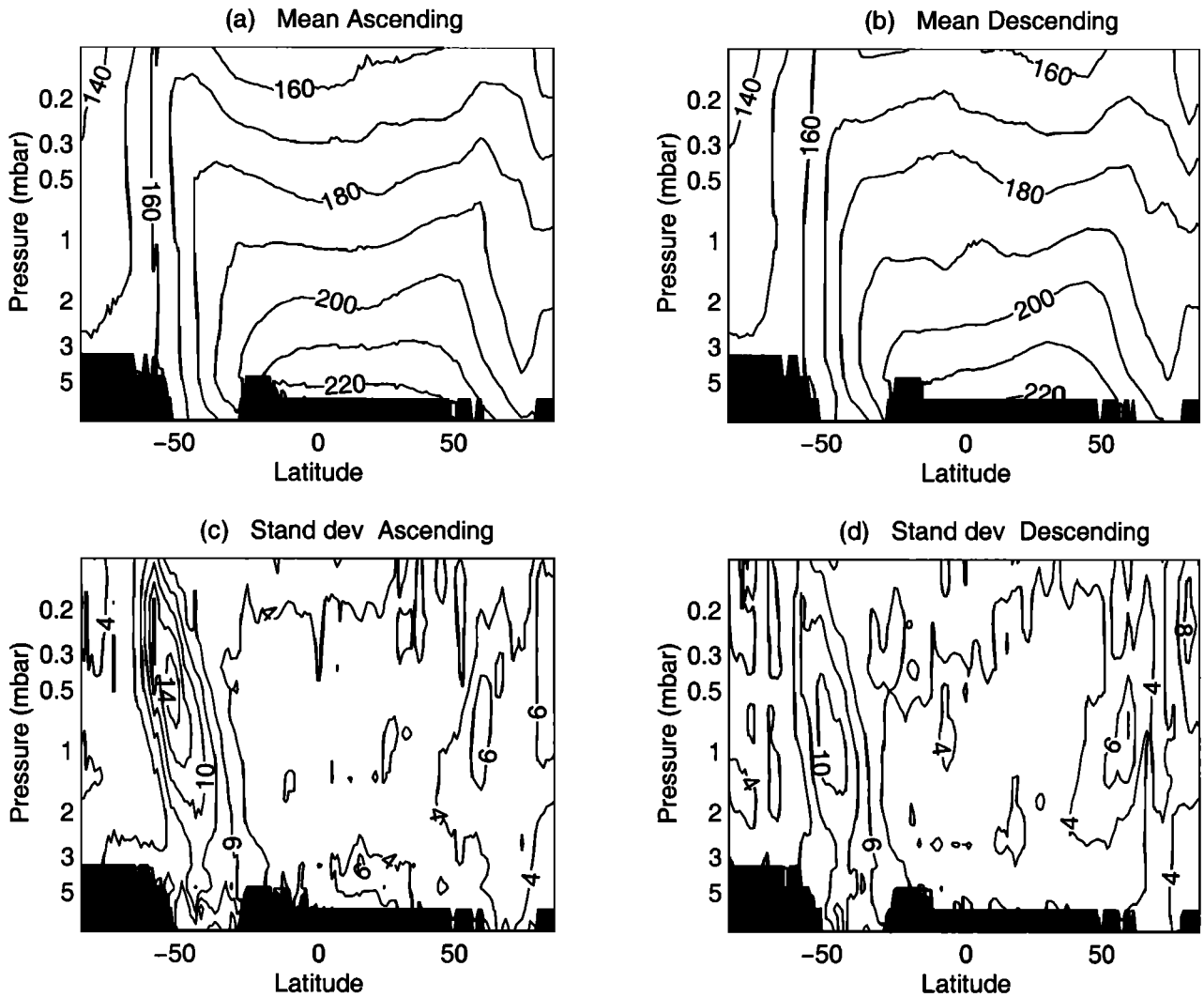

Figure 8. Zonal mean and standard deviation of temperature sampled from assimilation T34F1 along (a and c) ascending tracks and (b and d) descending tracks. Units are °K. Black areas mark regions of no data.

zonal velocity, and meridional velocity for the entire atmosphere in baseline simulation T34F0. The atmosphere was averaged over the 10-sol period before the zonal means were taken. Figure 7a represents features similar to those of Figures 4a and b, except data at all grid points are considered here rather than only for those along the trajectories of the orbits. The fact that Figure 7a is less noisy illustrates the artifacts introduced by the sampling strategy. Strong westerlies are seen along the polar front, with a maximum of 120 m/s at the top level of the model. Easterlies exist south of the westerlies and centered at the top level as well. The maximum in meridional velocity is found at the top of the atmosphere in low and middle latitudes.

4. Assimilation of TES Data Into MGCM

The observations and simulation agree with each other to a large degree; however, as we have seen in the previous section, there are discrepancies. The challenge we undertake here is to find out how much closer we can bring the model results to the observations, and to determine what the strengths and weaknesses of the model and of the current assimilation method are.

4.1. Assimilation Technique

Four-dimensional data assimilation problems in systems with large numbers of variables (e.g., the atmosphere or ocean) have been approached using Kalman filtering or a variational/adjoint method. These can be viewed as two different algorithms to solve the same statistical problem of minimizing the model–data difference [*Courtier and Talagrand,* 1990]; however, the Kalman filter predicts the time evolution of the covariances as well as the fields. In general, the dimension of the covariance problem is so large as to make Kalman filtering totally intractable. For statistically steady state problems, however, both methods reduce to a form of optimal interpolation (which is simply linear

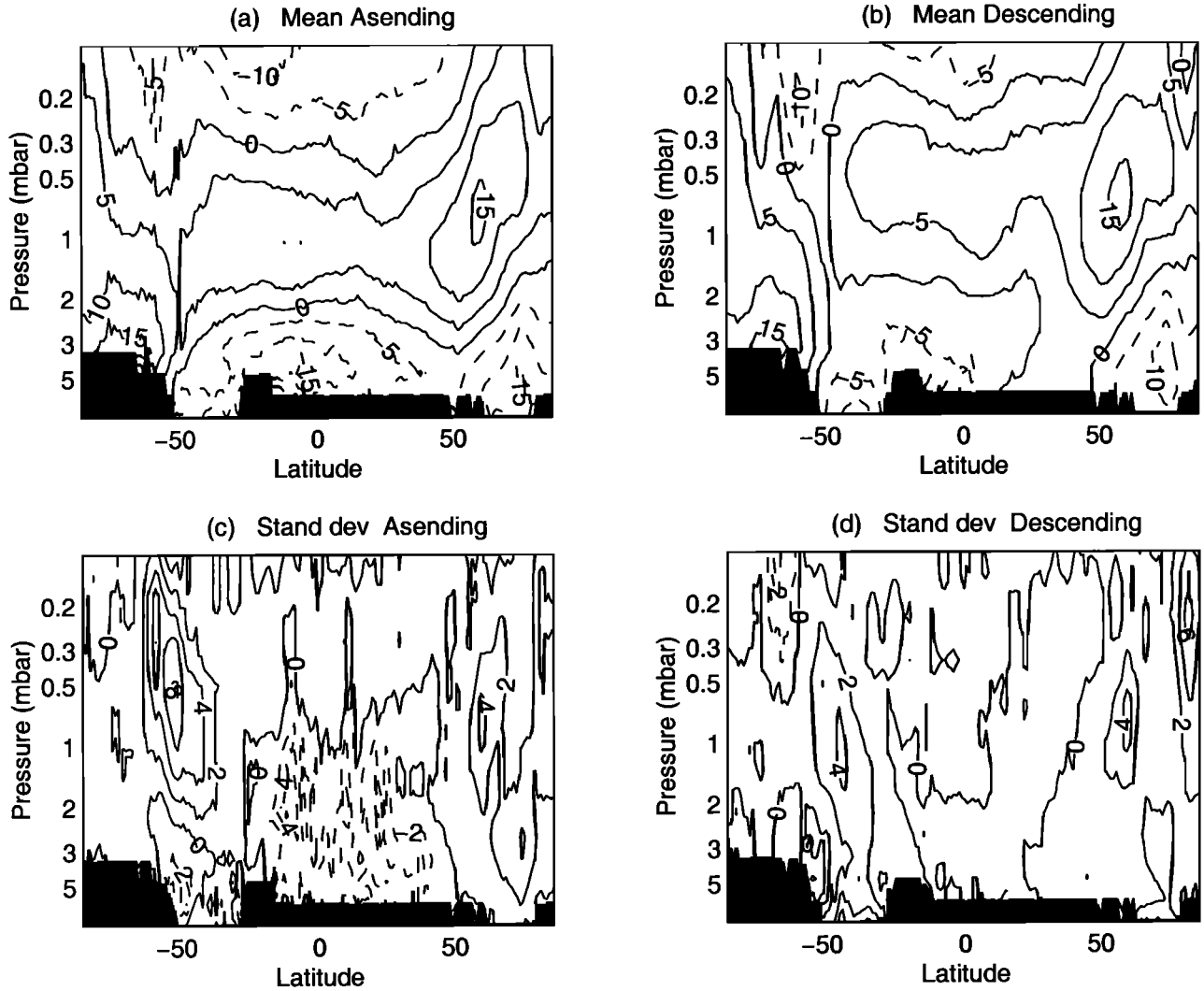

Figure 9. Difference in zonal means and standard deviations of temperature between assimilation T34F1 and observation, along (a and c) ascending tracks and (b and d) descending tracks. Units are °K. Black areas mark regions of no data.

regression), with the Kalman filtering estimating a gain matrix from the covariances rather than using a-priori choices for the correlations. The approach taken here is a steady-state Kalman filter [*Banfield et al.*, 1995].

$$\phi_k^a - \phi_k^p = \sum_{j=1}^{13N_t} \frac{f}{N_t} \cdot \alpha_{kj}(\phi_j^o - \phi_j^p)$$

where ϕ is a state variable (temperature); superscripts a, o, and p represent analysis, observation, and prediction, respectively. N_t is the number of profiles to be assimilated at time t. The model and the data are gridded to thirteen points in the vertical; the j represents one of the $13N_t$ data values. The model field is interpolated horizontally to the data location to give ϕ_j^p. The gain matrix α_{kj} determines how an individual data point affects all of the $13N_{lat}N_{lon}$ model grid points. The parameter f is empirically chosen to avoid the calculation becoming unstable.

To minimize the errors in the analysis state vector, the gains for grid point k are the solution to the following equation:

$$\sum_{j=1}^{N} (\overline{\epsilon_i^p \epsilon_j^p} + \overline{\epsilon_i^o \epsilon_j^o})\alpha_{kj} = \overline{\epsilon_k^p \epsilon_i^p}$$

where the quantities $\overline{\epsilon_i^p \epsilon_j^p}$ and $\overline{\epsilon_i^o \epsilon_j^o}$ are the covariances of the temperatures at positions i and j from the model prediction and the observations, respectively. On the right-hand side are the covariances between the model temperature at a grid point and at the data point. N is the number of total observational points, $13\sum_t N_t$, and the overbars indicate ensemble averages. The total size of this problem is $13N_{lat}N_{lon}N_{time\ steps} \times 13\sum_t N_t$.

We now make a series of assumptions to reduce the problem to a tractable dimension:

1. The gains are taken to be independent of time, except for a day-night difference.

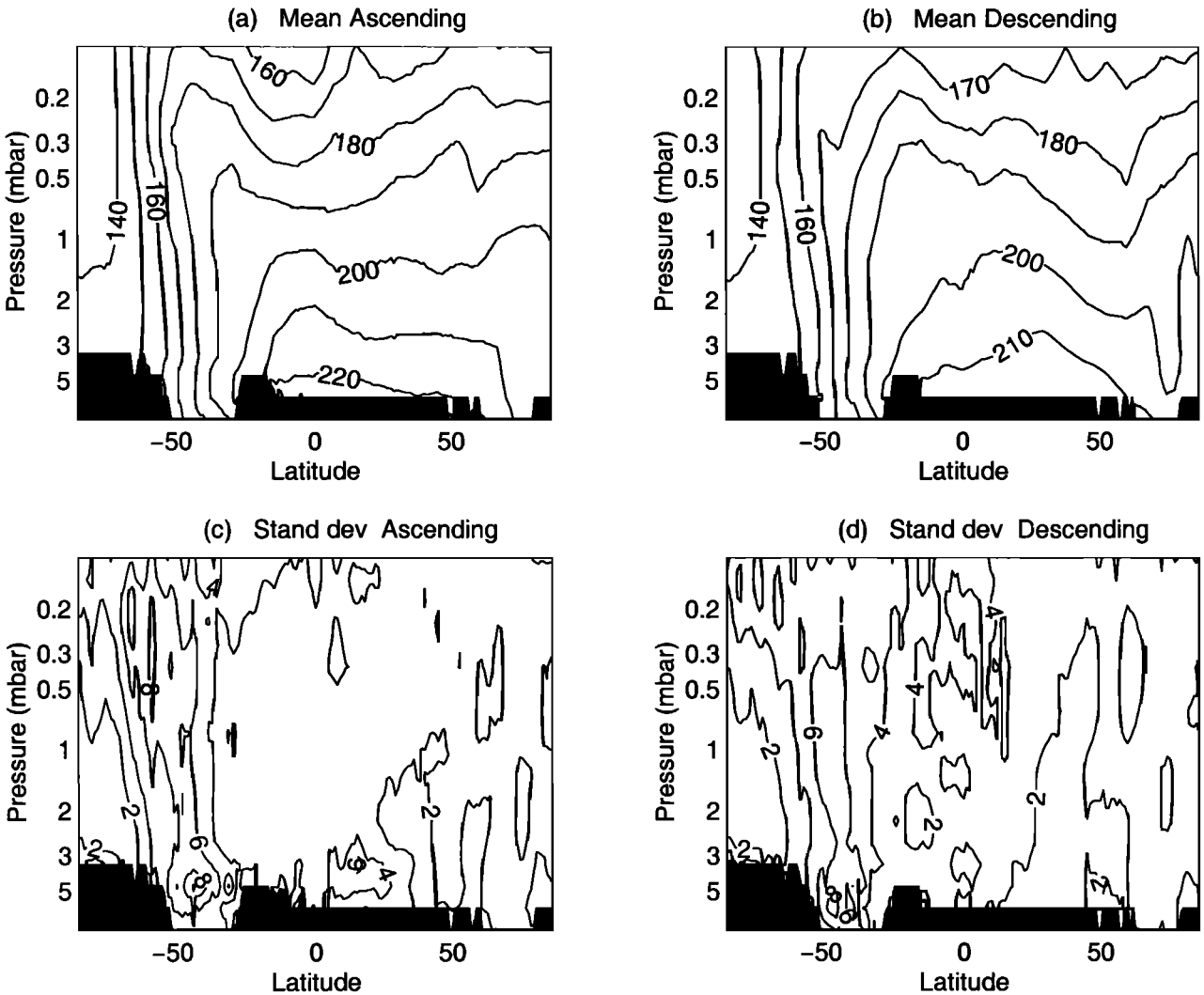

Figure 10. Zonal means and standard deviations of temperature values sampled from assimilation T72F1 along (a, c) ascending tracks, and (b, d) descending tracks. Units are °K. Black areas mark regions of no data.

2. The data are assumed to be uncorrelated horizontally and in time.

3. In the vertical, the covariances in the data are assumed to depend only the two neighboring heights above and below, with weights of 0.07, 0.24. 0.38, 0.24, and 0.07.

4. The gain depends only on the difference in longitude.

With these assumptions, the gain matrix becomes $2 \times N_{lat}^2 N_{long} \times 13^2$.

4.2. Assimilated Results

The assimilation using τ=0.34 and f=0.1 (hereinafter referred to as assimilation T34F1) was sampled along the trajectories of observations as in Figures 3 and 4, then the sampled data were zonally averaged and standard deviations associated with the zonal means were calculated (Figure 8). The maximum atmospheric temperature just above the ground is still smaller than the observations (Figure 3), and the tropospheric temperature lapse rate in the assimilated field remains lower than observations. Compared with simulation T34F0 (Figure 4), one can notice that at high latitudes of the summer hemisphere, the isotherms were brought down toward the ground. The difference between assimilation T34F1 and observations was plotted in Figure 9. The misfit has been reduced overall, compared to Figure 5, the size of the maximum at the north pole has decreased, so has the one at the top of the atmosphere above the equator. However, the misfit has increased by 5° at the ground level inside the polar vortex. The largest discrepancies in standard deviations are found in the polar front at 0.5 mbar and 1 mbar level for ascending and descending tracks, respectively. They are lower than that in the direct simulations, suggesting that the assimilation did succeed in pulling the high waves ac-

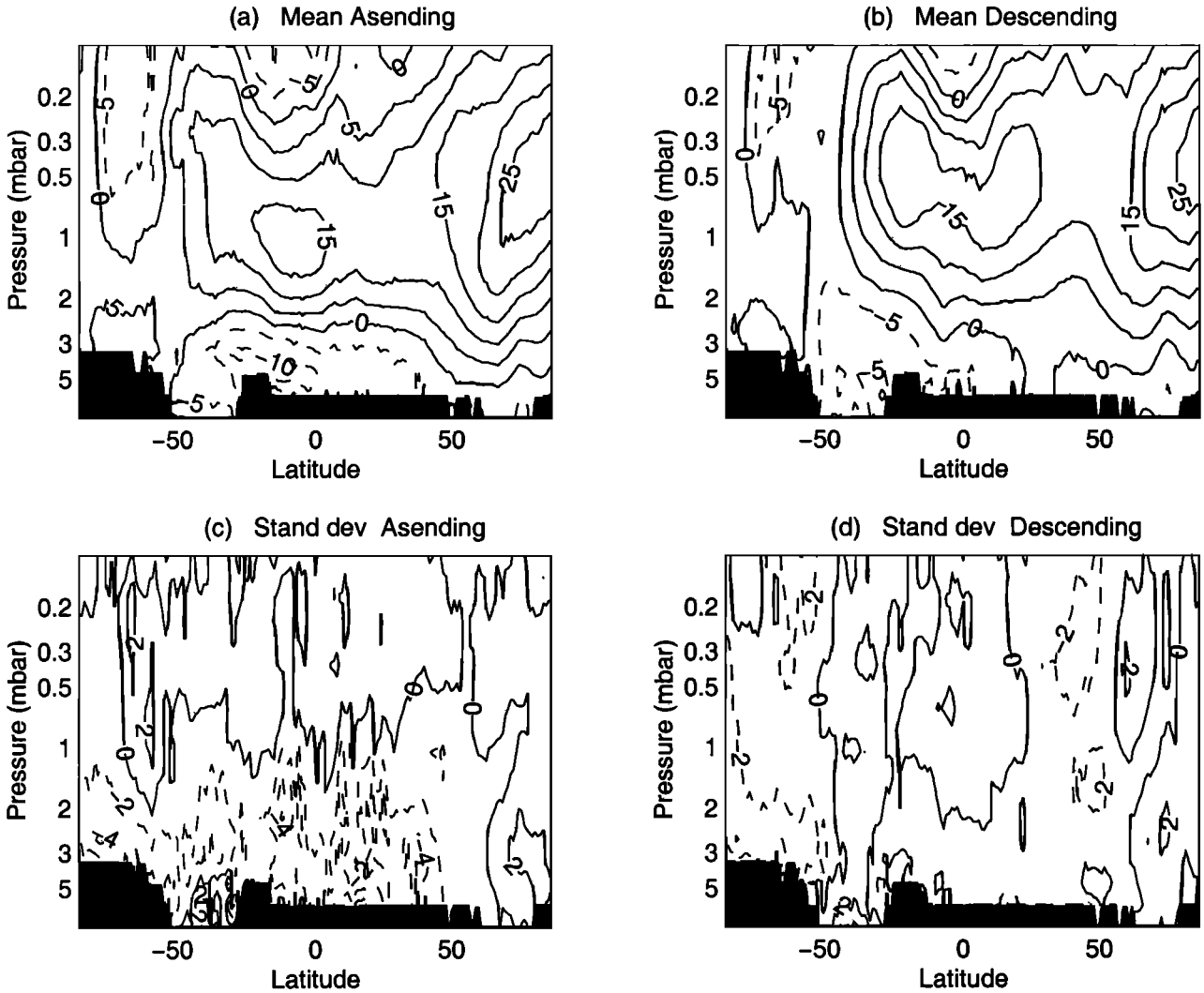

Figure 11. Difference in zonal means and standard deviations of temperature between assimilation T72F1 and observation along (a and c) ascending tracks and (b and d) descending tracks. Units are °K. Black areas mark regions of no data.

tivities toward the ground; however, they are still much higher than those in the observations.

We repeated the previous experiment with a higher dust value τ=0.72 (T72F1 hereafter); the zonally averaged temperatures and standard deviations, as well as the difference from the observations were plotted in Figure 10 and Figure 11, respectively. The misfit with the observations has increased near 1 mbar level and over the north pole, compared to Figure 9, but decreased inside the polar vortex and at the top and bottom of the atmosphere. However, the high activities have moved downward to a similar height as in the observations, and the magnitude is comparable too.

An assimilation using a third dust opacity τ=0.68 was performed. The RMS difference between the assimilated temperature and observations was calculated and plotted in Figure 12. Better agreement with the observations is achieved near the ground for higher dust opacities. On the other hand, better agreement is found above 2 mbar level for lower dust opacities, except above .2 mbar level where the accuracy of the retrieval is lower. These results are consistent with those from the simulations, suggesting the vertical distribution of dust opacity in the model should be reconsidered.

We have been looking at temporal averages so far; now we examine the temporal changes. Model results sampled on data in layer 9 (1 mbar level) during the last 15 hours of the 10-sol period were plotted against latitude in Plate 1a for all longitudes, and same results from the last 7 hours were plotted against time in Plate 1b for all latitudes and longitudes. Although the simulated temperature follows the mean value of the observations reasonably well, it fails to reproduce the downward slope at 50°N. While the assimilated temperature is systematically warmer than the observations, it succeeds in reproducing the temperature drop between 50°N and 80°N. In addition, Plate 1b illustrates that assimilation allows to catch the variations in time in

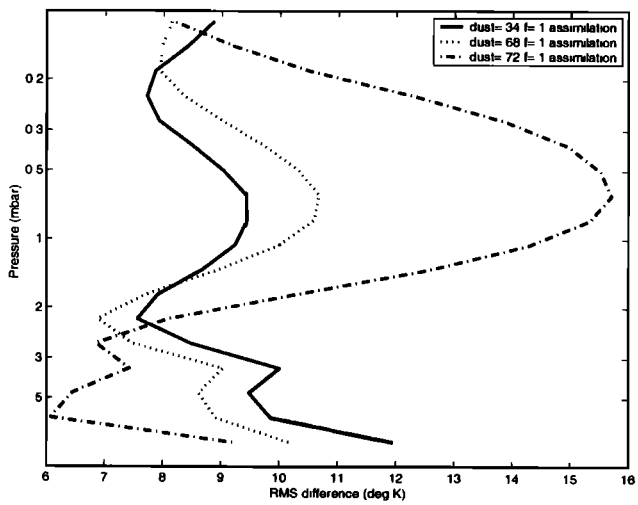

Figure 12. Temperature RMS difference between assimilations and observations as a function of pressure. The RMS is computer over longitude and latitude. The RMS is computed over longitude and latitude. The solid line is for assimilation T34F1, the dotted line is for assimilation T68F1, and the dash-dotted line is for assimilation T72F1. Note that all the assimilations used f=0.1.

the observations although it may have somewhat overreacted.

The zonal means of temperature, zonal velocity, and meridional velocity for the entire 10-sol averaged atmosphere in assimilation T34F1 (after one 10-sol series of TES data were assimilated) were plotted in Figure 13. The difference with simulation T34F0 is shown in Figure 14. Since the assimilation and the simulation start from the same initial state, these figures also give the tendencies of respective quantities. The meridional variations of isotherms in the assimilation looks much more similar to the observations than the simulation, especially at high altitudes near the north pole. The tendency for isotherms to rise monotonically with latitude near the north pole has been reversed. In the velocity field the westerlies have weakened, and the easterlies have strengthened and expanded downward. These changes are directly connected to the changes in the temperature field through the thermal wind equation, and the reversal of the isotherms at the north pole has generated easterly winds as fast as 60 m/s. Another noticeable change in the zonal velocity is the increment of 40 m/s at the top of the polar front, which is associ-

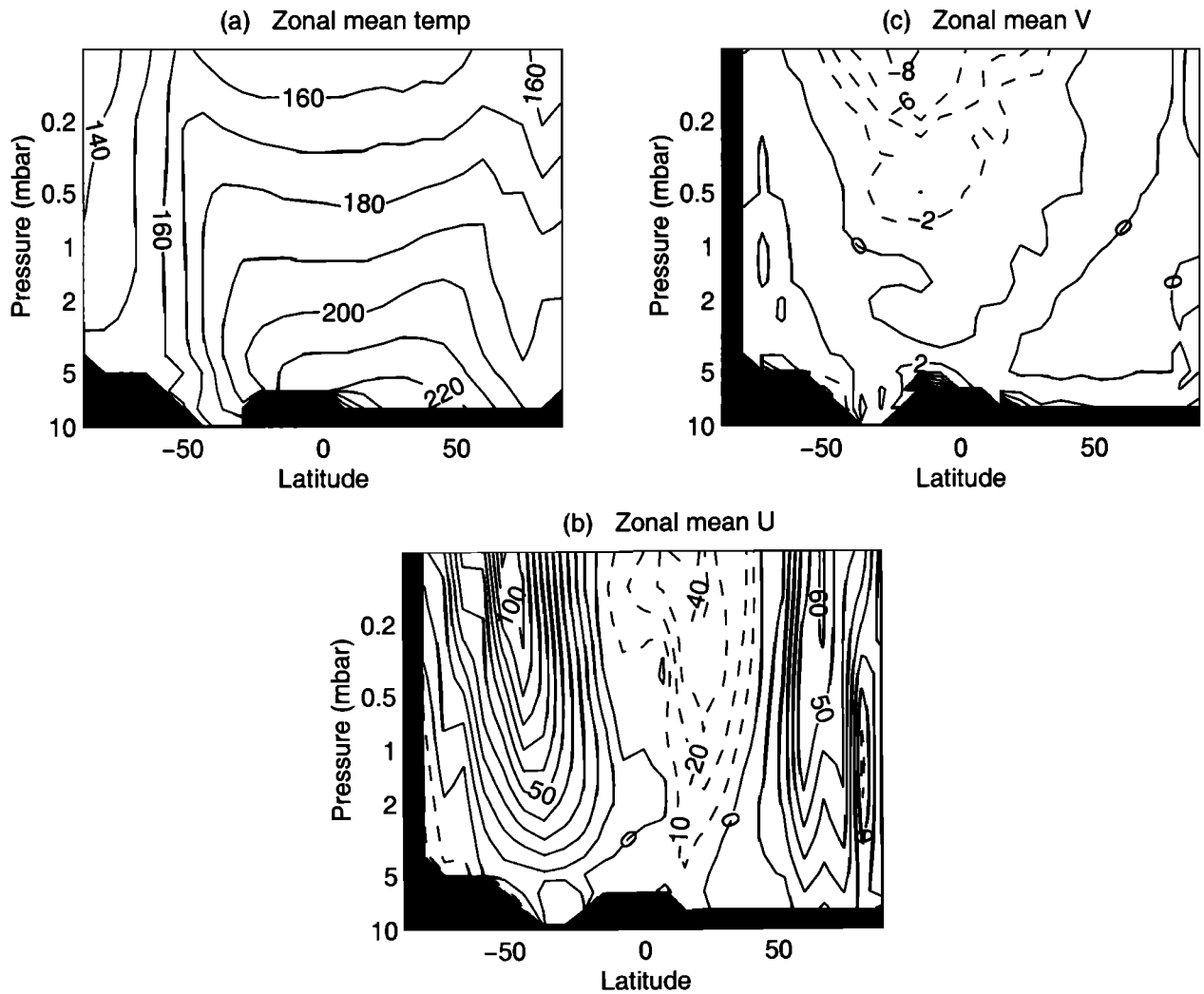

Figure 13. Zonally averaged (a) temperature, (b) zonal velocity, and (c) meridional velocity for the entire 10-sol mean atmosphere in assimilation T34F1. Black areas mark regions of no data.

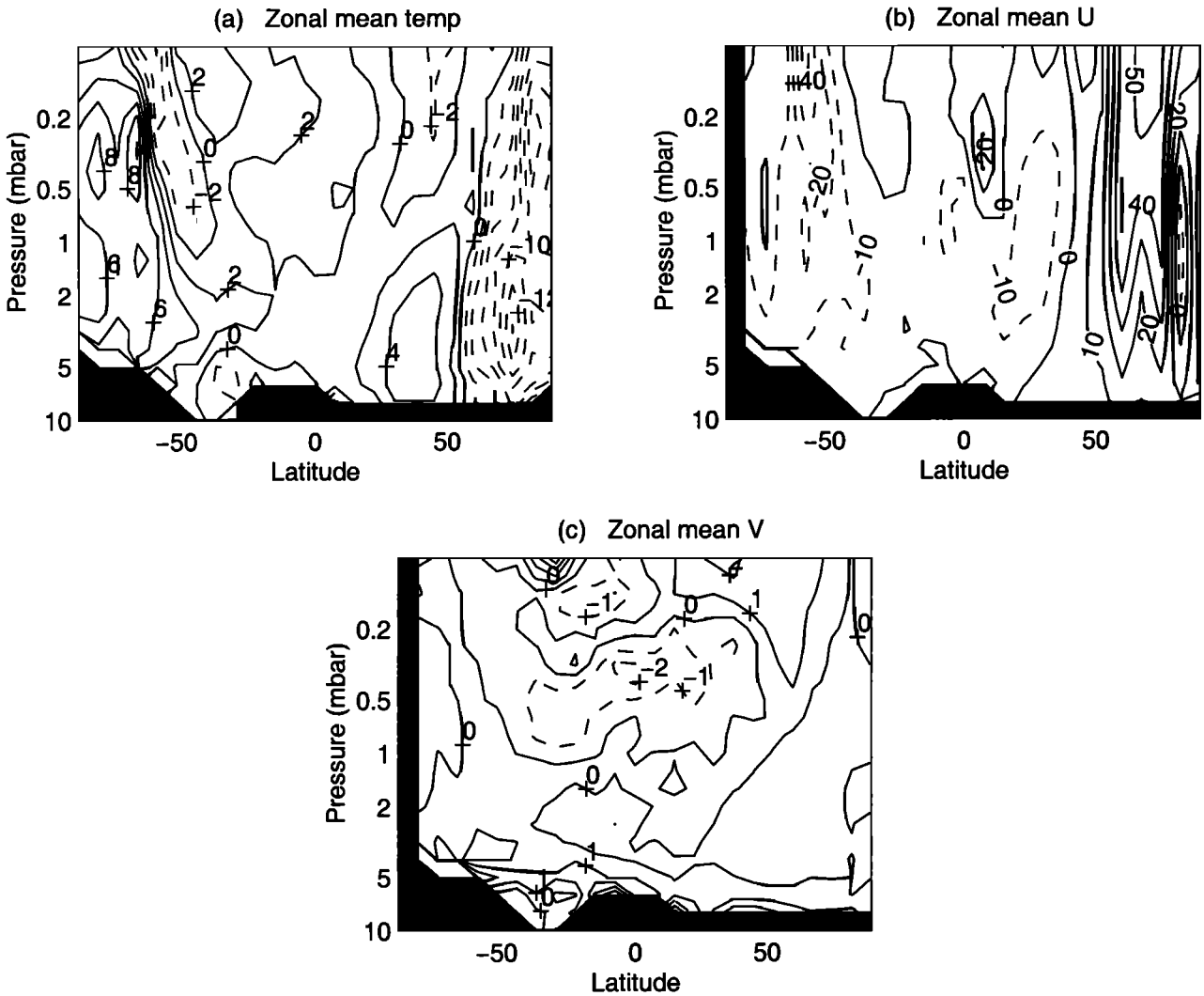

Figure 14. Difference in zonal means of (a) temperature, (b) zonal velocity, and (c) meridional velocity between 10-sol means of assimilation T34F1, after the 10-sol TES data are assimilated into the model, and direct simulation T34F0. Black areas mark regions of no data.

ated with the strengthening of the temperature gradient there. The meridional wind has basically remained the same and expanded downward slightly. Since we do not have observations of the wind field, we rely on the MGCM to provide the connections to the temperature field. Because assimilation has improved temperature structure there, it makes sense to conclude that the zonal wind over the north pole is closer to 60 m/s in reality than 0 m/s.

5. Discussion

Does the assimilation do a better job than the simulation? The RMS difference with the observations for simulation T34F0 and assimilation T34F1 were calculated first, then the difference between these error measures was taken and plotted in Plate 2a. Positive values indicate that the assimilation T34F1 is in better agreement with the observations. The improvement by the assimilation was achieved at four locations: 1) at the top of the atmosphere and 2) near the ground between 50°S and 50°N, 3) at northern high latitudes above the 3 mbar pressure level, and 4) in the polar front above 1 mbar pressure level. The assimilation does a worse job inside the polar vortex, in the middle atmosphere at low and middle latitudes, and at the north pole between the surface and 2 mbar pressure level. Plate 2b represents the difference between simulations T72F0 and T34F0; the generally positive values indicate that simulation T34F0 is in better agreement with the observations. Using the measured dust opacity gives better agreement in most parts of the atmosphere, except at the top and bottom in low and middle latitudes.

The empirical parameter f was first used by *Banfield at al.* [1995]; its maximum value is 0.2 in the current studies. The RMS difference for four f values was plotted in Figure 15. The assimilation using the current set of gains seems to bring the atmosphere closer to the observations in the upper atmosphere, but to drive it farther away at lower levels. The transition occurs slightly above 0.7 mbar pressure level.

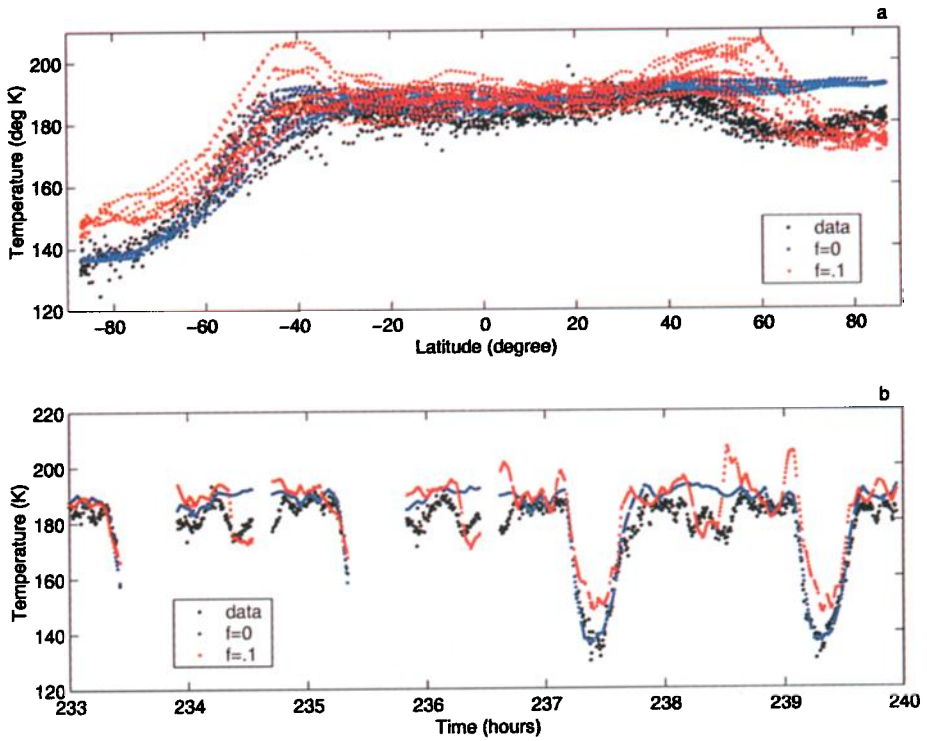

Plate 1. Temperatures of layer 9 (1 mbar level): (a) latitudinal variation during the last 15 hours and (b) temporal variations during the last 7 hours. Note all the data during that interval are considered since only one profile is sampled at a particular time. Black dots represent observational results, blue dots represent baseline simulation T34F0, and red dots represent assimilation T34F1.

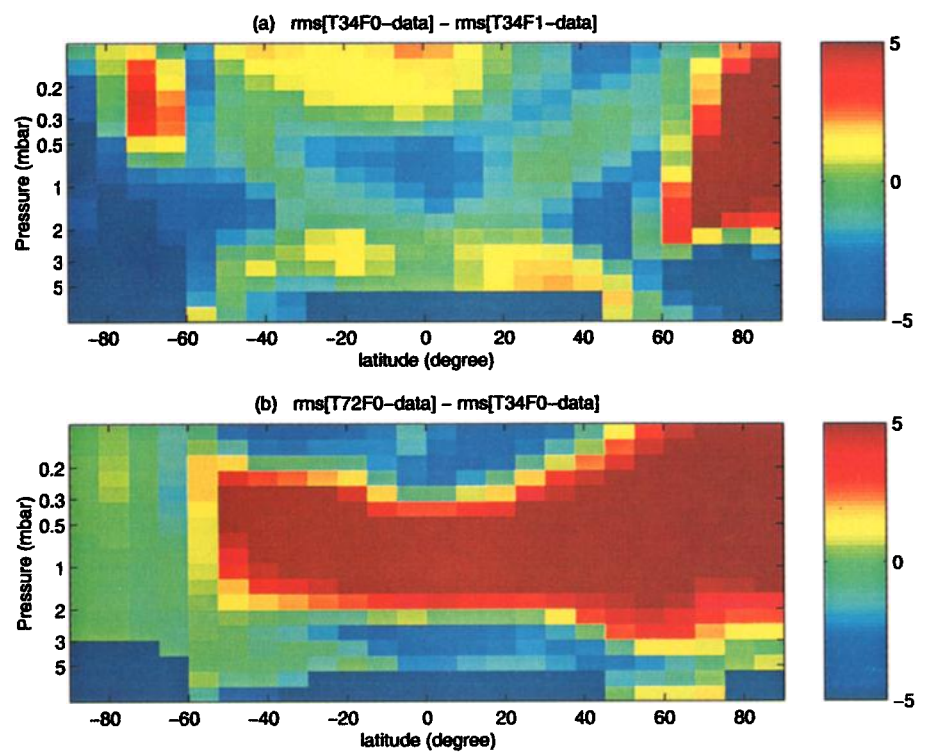

Plate 2. Comparisons in zonal mean of RMS difference between numerically calculated temperature and observations. (a) RMS difference between simulation T34F0 and data, subtracted by RMS difference between assimilation T34F1 and data. A positive value indicates improvement of assimilation over simulation. (b) RMS difference between simulation T72F0 and data, subtracted by RMS difference between simulation T34F0. Positive values indicate that simulation T34F0 is in better agreement with the observations.

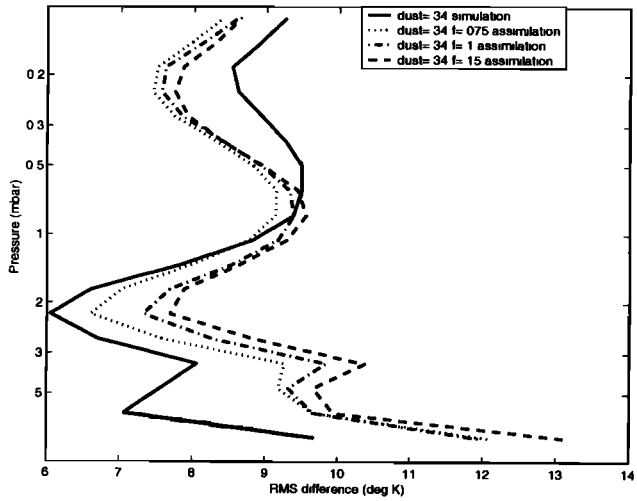

Figure 15. Temperature RMS difference between numerical solutions and observations as a function of pressure. The RMS is computed over longitude and latitude. The solid line is for simulation T34F0, the dotted line is for assimilation T34F075, the dash-dotted line is for assimilation T34F1, and dashed line for assimilation T34F15. Note that all of them use the same dust value: τ=0.34.

6. Conclusions

We have assimilated a set of 10-sol temperature profiles retrieved from TES radiance data during the MGS mapping phase into the Ames MGCM. We have sampled the baseline simulations and assimilations along the trajectories of the spacecraft and compared the model results with the observed temperature profiles. Preliminary results have shown that both the baseline simulations and assimilations are sensitive to the dust opacity. The current vertical distribution of dust does not lead to improvements of temperature at all vertical levels. More weight should be given to the dust in the lower atmosphere in order to get the correct tropospheric lapse rate and lead to improvement of temperature over the whole atmosphere.

The steady state Kalman filter as implemented here does offer improvement in the assimilated state. One example of the improvement by assimilation is the elimination of the northward rising trend of the isotherms in the northern polar region. It has drastic impact on speeding the zonal wind by 60 m/s. The assimilation does improve the representation of wave activities, however, the improvement is limited and not entirely satisfactory. It degrades the model results by warming up the temperatures south of 50°S between the surface and the 1 mbar level, that were already too warm in the direct simulation. This is because the dust opacity should be reconsidered as 5 times larger at the south pole than at the equator like in data (see Figure 2) instead of being uniformly distributed like in the model. In addition, the increase of opacity at the south pole should take place at some high place above the surface for the model surface temperature to be warmer. This is also consistent with the fact that there is a strong polar vortex there.

Acknowledgments. We are indebted to all the engineers and scientists who worked on the mission of MGS, as well as those who are involved in routine operations of data management. We thank the two anonymous reviewers for their constructive comments.

References

Christensen, P. R., et al., Thermal Emission Spectrometer Experiment: Mars Observer Mission, *J. Geophys. Res., 97*, 7719-7734, 1992.

Christensen, P. R., et al., Results from the Mars Global Surveyor Thermal Emission Spectrometer, *Science, 279*, 1692-1698, 1998.

Banfield, D., A.P. Ingersoll, and C.L. Keppenne, A steady-state Kalman filter for assimilating data from a single polar orbiting satellite, *J. Atmos. Sci., 52*, 737-753, 1995.

Conrath, B. J., J. C. Pearl, M. D. Smith, W. C. Maguire, P. R. Christensen, S. Dason, and M. S. Kaelberer, Mars Global Surveyor Thermal Emission Spectrometer (TES) observations: Atmospheric temperatures during aerobraking and science phasing, *J. Geophys. Res, 105*, 9509-9520, 2000.

Courtier, P., and O. Talagrand, Assimilation of meteorological observations: A review of present problems, paper presented at International Symposium on Assimilation of Observations in Meteorology and Oceanography, World Meteorol. Org., Clermont-Ferrand, France, July 1990.

Harberle, R. M., J. B. Pollack, J. R. Barnes, R. W. Zurek, C. B. Leovy, J. R. Murphy, H. Lee, and J. Schaffer, Mars atmospheric dynamics as simulated by the NASA Ames general circulation model, 1, the zonal-mean circulation, *J. Geophys. Res., 98*, 3093-3123, 1993.

Kass, D. M., Changes in the Marian atmosphere, doctoral dissertation, Calif. Inst. of Technol., Pasadena, Calif., 1999.

Pollack, J. B., R. M. Haberle, J. Schaffer and H. Lee, Simulation of the general circulation of the Martian atmosphere, 1, Polar processes, *J. Geophys. Res., 95*, 1447-1473, 1990.

Smith D. E., et al., The global topography of Mars and implications for surface evolution, *Science, 284*, 1495-1503, 1999.

Smith, M. D., J. C. Pearl, B. J. Conrath, and P. R. Christensen, Mars Global Surveyor Thermal Emission Spectrometer (TES) observations of dust opacity during aerobraking and science phasing, *J. Geophys. Res., 105*, 9539-9552, 2000a.

Smith, M. D., J. L. Bandfield, and P. R. Christensen, Separation of atmospheric and surface spectral features in Mars Global Surveyor Thermal Emission Spectrometer (TES) spectra, *J. Geophys. Res., 105*, 9589-9608, 2000b.

B. J. Conrath, J. C. Pearl, and M. D. Smith, MS 693-0, NASA Goddard Space Flight Center, Greenbelt, MD 20771.

R. M. Haberle, Space Science Division, MS 245-3, NASA Ames Research Center, Moffett Field, CA 94035.

A. P. Ingersoll, Division of Geology and Planetary Sciences 150-21, California Institute of Technology, Pasadena, CA 91125.

D. M. Kass, MS 169-237, Jet Propulsion Laboratory, 4800 Oak Grove Drive, Pasadena, CA 91109.

K. Q. Zhang, Ocean Science Element, MS 300-323, Jet Propulsion Laboratory, 4800 Oak Grove Drive, Pasadena, CA 91109. (katez@pacific.jpl.nasa.gov)

(Received July 19, 2000; revised May 21, 2001; accepted May 25, 2001.)